

# **Visualization of subsurface nanoparticles in polymer matrix using resonance tracking atomic force acoustic microscopy and contact resonance spectroscopy**

Kuniko Kimura<sup>1)</sup>, Kei Kobayashi<sup>1,2)</sup>, Atsushi Yao,<sup>1)</sup> and Hirofumi Yamada<sup>1)</sup>

<sup>1)</sup>Department of Electronic Science and Engineering, Kyoto University, Kyoto 615-8510, Japan

<sup>2)</sup>The Hakubi Center for Advanced Research, Kyoto University, Kyoto 615-8520, Japan

## **Abstract**

A visualization technique of subsurface features with a nanometer-scale spatial resolution is strongly demanded. Some research groups have demonstrated the visualization of subsurface features using various techniques based on atomic force microscopy. However, the imaging mechanisms have not yet been fully understood. In this study, we demonstrated the visualization of subsurface Au nanoparticles buried in a polymer matrix 900 nm from the surface using two techniques; i.e., resonance tracking atomic force acoustic microscopy and contact resonance spectroscopy. It was clarified that the subsurface features were visualized by the two techniques as the area with a higher contact resonance frequency and a higher  $Q$ -factor than those in the surrounding area, which suggests that the visualization is realized by the variation of the contact stiffness and damping of the polymer matrix due to the existence of the buried nanoparticles.

## 1. Introduction

A nondestructive visualization technique of subsurface features with a nanometer-scale spatial resolution is strongly demanded in many scientific research fields such as nanoelectronics, nanomechanics, and life science. Atomic force microscopy (AFM) has been proven to be an excellent visualization technique for surface features and properties with a nanometer-scale spatial resolution. Some research groups have demonstrated the visualization of subsurface features using various techniques based on AFM [1-13]; i.e., ultrasonic AFM (UAFM) [6,12], atomic force acoustic microscopy (AFAM) [1,8,10], heterodyne force microscopy (HFM) [3-5,7,13], and ultrasonic force microscopy (UFM) [9]. Recently, we also reported the visualization of Au nanoparticles buried almost 1  $\mu\text{m}$  from the surface of a polymer matrix by HFM and AFAM [14].

In UAFM, the cantilever base is excited at a single drive frequency ( $f_d$ ) chosen near the contact resonance frequency ( $f_c$ ) of the cantilever, and the cantilever oscillation at  $f_d$  is detected [6,12,15]. On the other hand, in AFAM, the sample is excited at  $f_d$  by a piezoelectric actuator underneath the sample [1,8,10,16,17]. In HFM, both the sample and cantilever base are excited at high frequencies,  $f_1$  and  $f_2$ , respectively, which are typically on the order of MHz, and the cantilever oscillation at the beat frequency ( $|f_1 - f_2|$ ) near  $f_c$  is detected [3-5,7,13,18]. On the other hand, in UFM, the actuator beneath the sample is excited by an amplitude-modulated high frequency signal with a modulation frequency ( $f_m$ ) chosen near  $f_c$ , and the cantilever oscillation at  $f_m$  is detected [9,19].

Since these techniques commonly utilize the contact resonance of the cantilever with its tip in contact to the sample surface, the mechanisms of subsurface feature visualization are presumably associated with the variation in the contact resonance. The contact resonance is often characterized by the resonance frequency ( $f_c$ ) and the mechanical  $Q$ -factor, which are closely related to the contact stiffness and damping [10,17]. However, in previous reports on subsurface feature visualization except for that by Killgore *et al.*[10], only the amplitude and phase at a single frequency near  $f_c$  were measured, and it is difficult to separately assess the effect of the contact stiffness and damping on the imaging mechanisms.

To elucidate the effect of the variations in the contact stiffness and damping on the subsurface visualization mechanisms, we employed two techniques based on AFAM to visualize the buried Au nanoparticles in the polymer matrix. The first technique is resonance tracking AFAM (RT-AFAM), in which a phase-locked loop (PLL) is utilized to directly measure  $f_c$  and the oscillation amplitude at the resonance during a raster scan. The setup is similar to those previously reported [20-22], which allows us to quickly obtain information about the contact stiffness and damping independently from the  $f_c$  and  $Q$ -factor channels, respectively. However, in this method, a sudden change in the surface mechanical properties can cause a shift in  $f_c$  greater than the track range of the PLL [23-25], then the PLL may not properly track  $f_c$  if there are spurious resonance peaks that distort the resonance spectrum [26,27]. A nonlinear tip-sample interaction can also cause distortion and bifurcation in the resonance spectrum [17,28,29], which could be problematic for evaluating the contact stiffness and damping. Therefore, we employed another technique, AFAM contact resonance spectroscopy (AFAM-CRS), in which the amplitude and phase responses of the cantilever to a swept-sine excitation of the sample are collected at every pixel during a raster scan in order to evaluate the variations in the contact stiffness and damping in more detail as well as to confirm that the resonance spectra are not distorted. This method has been applied for the analyses of the surface viscoelastic properties [30-36]. As far as our knowledge, only one paper reported the application of this method for studying subsurface imaging mechanisms [10]. As this method provides the complete amplitude and phase data in the swept frequency range at every scanned pixel, we can reconstruct the AFAM amplitude and phase images at an arbitrary frequency in the swept frequency range.

In this paper, we show the RT-AFAM result and compare  $f_c$  and the resonance amplitude on the buried Au nanoparticles and those on the surrounding area. We then present the AFAM-CRS result to compare the contact resonance spectra in these areas. Finally, we discuss the visualization mechanisms of nanoparticles buried in the soft matrix based on the AFAM-related techniques.

## 2. Experimental

## 2.1 Sample preparation

A polyimide sheet (DuPont-Toray: Kapton 500V) with a thickness of 125  $\mu\text{m}$  was used as the substrate. The sheet was cut into a 30 mm  $\times$  30 mm piece, then cleaned in acetone and ethanol. The sheet was irradiated by UV light for 30 minutes to improve the wettability of the surface. A 10  $\mu\text{l}$  droplet of aqueous citric acid solution containing Au nanoparticles of 40 nm diameter (Tanaka Kikinzoku Kogyo) was dropped onto the polyimide sheet using a microsyringe in a clean room. After 2 minutes, the supernatant solution was removed using the microsyringe and the sheet was dried in the ambient air of the clean room. A photopolymer (Dow Electric Materials: Microposit S1813G) was spin-coated as a top-coat, and annealed at 130°C for 3 minutes. The cross-sectional SEM image of the sample was shown in our previous paper [14]. The thickness of the top-coat film was estimated to be 900 nm by measuring the thickness of the film on a Si wafer prepared in the same way using a surface profiler (KLA-Tencor: P-15).

## 2.2 Instruments and Cantilevers

We used a commercial AFM instrument (JEOL: JSPM 4200) after some modifications to the optics and electronics [37]. We used a digital lock-in amplifier (LIA) (Zurich Instruments: HF2LI) with PLL and multi-frequency (MF) options. The sample was directly glued on the top electrode of a lead zirconate titanate (PZT) piezoelectric actuator, which was fixed on a tube scanner. We used Si cantilevers (Nanosensors: PPP-ZEILR), whose spring constants ( $k_z$ ) were calibrated using Sader's method [38]. The nominal tip radius was less than 10 nm.

## 2.3 RT-AFAM

Figure 1 shows the experimental setup for the RT-AFAM. The setup is similar to that for the RT-UAFM [20-22]. After the tip was contacted to the sample surface, we measured the amplitude and phase spectra of the cantilever for the frequency range around the contact resonance by exciting the PZT actuator using a swept-sine signal with a constant excitation amplitude. From the amplitude

response curve, we first identified the contact resonance frequency at the initial contact point ( $f_{c0}$ ) as the frequency at which the maximum oscillation amplitude was recorded. The phase difference ( $\theta$ ) between the cantilever deflection signal and the excitation signal at  $f_{c0}$  was then set to  $\theta_0$ . After that, the PZT actuator was excited by a numerically controlled oscillator (NCO) in the PLL at  $f_{c0}$  with a constant excitation amplitude. While the tip was raster-scanned on the sample surface, the PLL kept  $\theta$  constant at  $\theta_0$ , and the shift in the contact resonance frequency from  $f_{c0}$  was recorded as the  $\Delta f$  image. The amplitude signal ( $R$ ) from the LIA was also recorded as the amplitude image. A single RT-AFAM measurement took approximately 5 min.

## 2.4 AFAM-CRS

Figure 2 shows the experimental setup for the AFAM-CRS measurements. The setup is similar to those reported earlier [30-36]. After identifying  $f_{c0}$ , at the initial contact point, the amplitude and phase spectra of the cantilever for the frequency range around the contact resonance were collected by exciting the PZT actuator using a swept-sine signal at every pixel, while the tip was raster-scanned. A swept-sine signal with a sweep frequency range of 25 kHz around  $f_{c0}$  was generated by a function synthesizer (NF: WF1974). The PLL was used to generate a synchronized swept-sine signal, which was used to excite the PZT actuator at a constant excitation amplitude, and the frequency of the NCO was set as the reference frequency in the LIA. During the frequency sweep, we recorded  $R$ ,  $\theta$ , and  $f$  using a data acquisition device to reconstruct the contact resonance spectrum at each pixel. The data points recorded during the single sweep were 350. During the resonance spectrum measurement, it is desirable to measure the amplitude and phase responses of the cantilever in a quasi-stationary manner at each frequency in the sweep frequency range. If the sweep rate is too fast, the measured resonance spectrum is distorted [39,40]. On the other hand, the tip-sample contact conditions may vary during a sweep at each pixel if the sweep rate is too slow and the resonance spectrum measurement takes, for example, more than one second. Therefore, we studied the relationship between the sweep time and the shape of the measured resonance spectrum, and

determined the sweep time for the AFAM-CRS measurement to be 175 ms (see Appendix A). After 5ms of data saving time, the tip was moved to the next pixel, and the same procedures were repeated for  $128 \times 128$  pixels. A single AFAM-CRS measurement took approximately 100 min.

### 3. Results and discussion

Figures 3(a)-(c) show the topography,  $\Delta f$ , and  $R$  images, respectively, obtained by the RT-AFAM. The scan area was  $500 \text{ nm} \times 500 \text{ nm}$ . During this measurement, the cantilever tip ( $k_z = 1.2 \text{ N/m}$ ) was contacted to the surface with the contact force of 13.8 nN, and  $f_{c0}$  was about 96 kHz. We found some bright spots in both the  $\Delta f$  and  $R$  images in the area, as indicated by the arrows “A”, “B”, and “C”, which correspond to the subsurface Au nanoparticles. Note that no particle feature was observed at the corresponding positions in the topography. Figures 3(d) and (e) are magnified images of the areas indicated by the solid squares in figures 3(b) and (c), respectively. Figures 3(f) and (g) are cross-sectional profiles measured along the solid lines indicated in figures 3(d) and (e). The  $\Delta f$  profiles show that  $\Delta f$  measured in the area with the subsurface Au nanoparticle was higher than that measured on the surrounding area by about 4 kHz. The  $R$  profile shows that the  $R$  measured in the area with the subsurface Au nanoparticle was about 1.3 times larger than that measured in the surrounding area. The histograms of  $\Delta f$  and amplitude are presented in Appendix B, in which the values of  $\Delta f$  and amplitude recorded at the pixels “A”, “B” and “C” are located far out of the broad peaks representing the values at the pixels without the nanoparticles underneath. Assuming a linear tip-sample interaction,  $f_c$  and  $R$  represent the variations in the contact stiffness and inverse of the viscosity, respectively. Therefore, the results suggest that the visualization of the subsurface Au nanoparticles by AFAM and related techniques are due to the variation in the contact stiffness and damping; the subsurface Au nanoparticles brought a higher surface contact stiffness and lower damping. In the next section, we show the AFAM-CRS results in order to discuss the variations in the contact stiffness and damping in more detail.

We performed the AFAM-CRS measurement in a scan area of  $1 \mu\text{m} \times 1 \mu\text{m}$  on the same

sample. In this measurement, a cantilever tip ( $k_z = 1.1 \text{ N/m}$ ) was contacted to the surface with the contact force of 25.6 nN. Since we found that  $f_{c0}$  was about 90 kHz, the start and stop frequencies were set as 75 kHz and 100 kHz, respectively. Figure 4(a) is a reconstructed AFAM amplitude image at 91.6 kHz for an area of  $500 \text{ nm} \times 500 \text{ nm}$ . Topographic image is available in Appendix B. The brightness represents the amplitude at 91.6 kHz in the contact resonance spectrum recorded at each pixel. We found a few bright spots that correspond to the subsurface Au nanoparticles as we observed in the RT-AFAM images and conventional AFAM amplitude and phase images [14]. We focused on the bright spot indicated by the arrow “1” in figure 4(a). The arrow “1” indicates the pixel that appeared the brightest in the image. We extracted the frequency spectrum at pixel “1”, and those at pixels “2” and “3” which were chosen on the scan line including pixel “1” with a spacing of about 135 nm as the representative pixels in the area without nanoparticles underneath. The amplitude and phase spectra of these pixels are shown in figures 4(b) and (c), respectively. The amplitude spectra on pixel “1” as well as those on pixels “2” and “3” are not skewed but almost symmetric, which allows us to use the linear approximation of the tip-sample interaction [17,29]. Figure 4(b) shows that the frequency of the maximum amplitude on pixel “1” was about 91.5 kHz, while those on the other pixels were about 90 kHz. Figure 4(c) also shows that the phase spectrum measured on pixel “1” was shifted in the direction of the higher frequency from those on pixels “2” and “3” by about 1.5 kHz. On the other hand, the maximum amplitude on pixel “1” was about 1.2 times greater than those of the other pixels. These results showed that the subsurface Au nanoparticle brought the contact stiffness and damping of the polymer surface higher and lower, respectively, which were consistent with the RT-AFAM results.  $f_c$  image and its histogram are also available in Appendix B.

To elucidate the influence of the excitation frequency in the AFAM, we show, in figure 5, the AFAM amplitude and phase images of the area with the subsurface nanoparticle reconstructed from the AFAM-CRS data at various frequencies ranging from 88.5 kHz to 93.0 kHz. Each image was constructed from the amplitude or phase data of  $30 \times 10$  pixels. They are shown in the same colour scale bar without any image processing. In the AFAM amplitude images, the subsurface feature in

the centre can be recognized as a dark spot in the frequency range from 88.5 kHz to 90.0 kHz, then it becomes barely visible in the range of 90.0 kHz and 91.5 kHz, and becomes again visible but as a bright spot in the range from 91.5 kHz to 93.0 kHz. The contrast in the AFAM images depends on the excitation frequency, and it is even inverted as shown here, thus care must be taken to interpret the AFAM amplitude images [41]. On the other hand, the reconstructed AFAM phase images consistently show the subsurface feature as bright spot in the frequency range from 90.0 kHz to 91.5 kHz.

We discuss the influence of the subsurface nanoparticle on  $f_c$  and the  $Q$ -factor measured on the pixels above the subsurface nanoparticle. As presented in an illustration of figure 6(a), the subsurface nanoparticle is supposed to exist just beneath the brightest pixel “1” in figure 4(a). Figure 6(b) is a magnified AFAM amplitude image reconstructed from AFAM-CRS data at 91.6 kHz around the pixel “1”, which is represented by the same colour scale bar as that of figure 5. As illustrated in figure 6(a), the spacing of the data pixel in the scan line was 7.8 nm, and the number of pixels within the circle with a diameter of 40 nm from pixel “1” is 5. The nearest neighbour pixels on the left and right of pixel “1” are labeled as “A<sub>L</sub>” and “A<sub>R</sub>”, respectively. The next neighbour ones are labeled as “B<sub>L</sub>” and “B<sub>R</sub>”, respectively. The five pixels of interest were enclosed with the rectangle in figure 6(b), in which a circle representing the size of the Au nanoparticles was also drawn with the centre at pixel “1”. The amplitude spectra recorded on these five pixels and pixel “2” in figure 4 are shown in figures 6(c)-(h) after processing with a 5-point simple moving average filter. We fitted these amplitude spectra with that of the simple harmonic oscillator (SHO), namely  $R = A_0 / ((1 - (f/f_c)^2)^2 + (f/(f_c Q))^2)^{1/2}$ , where  $A_0$  is a constant, and obtained  $f_c$  and the  $Q$ -factor as the best fit parameters. We found that  $f_c$  and the  $Q$ -factor of pixels “1”, “A<sub>L</sub>”, and “A<sub>R</sub>” were higher than those of pixel “2”, while those of pixels “B<sub>L</sub>” and “B<sub>R</sub>” were almost the same as those of the pixel “2”. Thus, the subsurface Au nanoparticle affects the contact stiffness and damping in the area whose diameter is smaller than that of the Au nanoparticle, which was consistent with our previous study [14].



The AFAM-CRS results again indicate that the contact stiffness and damping on the area with the Au nanoparticle underneath was higher and lower, respectively, due to the existence of the Au nanoparticles. Based on these results, we presume that the contact stiffness and damping measured by the RT-AFAM and AFAM-CRS techniques are not only determined by the surface characteristics, but affected by the Au nanoparticles buried 900 nm from the polymer surface. As all the amplitude spectra were well fitted to the SHO model, the distortion due to the nonlinear tip-sample interaction and spurious resonance peaks were negligible in the frequency range of concern. This not only affirms that the discussion based on the RT-AFAM result was valid but also allows us to estimate the variations in the elasticity of the polymer surface caused by the subsurface Au nanoparticle as follows.

We estimated the variation in the elasticity of the polymer surface caused by the subsurface Au nanoparticle. We fitted the amplitude spectra recorded at the pixels “1” and “2” in figure 4(a) with that of the cantilever whose tip at its end in contact to the surface with a spring representing contact stiffness ( $k^*$ ) and dashpot representing damping ( $\gamma$ ) in parallel (Voigt model), namely the theoretical AFAM amplitude spectrum  $R = c|\kappa(k^* + i\gamma\omega)(\sin\kappa L \sinh\kappa L)/(k_z(\kappa L)^3(1 + \cos\kappa L \cosh\kappa L) + 3(k^* + i\gamma\omega)(\cosh\kappa L \sin\kappa L - \sinh\kappa L \cos\kappa L))|$ , where  $c$ ,  $\kappa$  and  $L$  are a constant, the wavenumber and the length of the cantilever [22,42].  $\kappa$  can be calculated from the experimentally measured values of  $f_c$  as  $\kappa = 1.8751(f_c/f_0)^{1/2}$ , where  $f_0$  is the first free resonance frequency of the cantilever and 1.8751 is the dimensionless wavenumber of the free first resonance [28]. We obtained the contact stiffness and damping as the best fit parameters;  $k^*$  on the area with and without a Au nanoparticle underneath were calculated to be 42 N/m and 38 N/m, respectively, while  $\gamma$  on both pixels were about  $3.9 \times 10^{-6}$  Ns/m. We use the Hertzian model, and the reduced Young's moduli ( $E^*$ ) is given by  $E^* = (k^{*3}/(6R_t F_n))^{1/2}$ , where  $R_t$  and  $F_n$  are the tip radius and normal loading force, respectively. By assuming  $R_t$  of 10 nm,  $E^*$  on the areas with and without Au nanoparticle underneath were calculated as 7.0 GPa and 5.9 GPa, respectively.  $E^*$  is defined as  $1/E^* = ((1-\nu_t^2)/E_t + (1-\nu_s^2)/E_s)$ , where  $E_{t(s)}$  and  $\nu_{t(s)}$  are the Young's modulus and the Poisson's ratio of the tip and the sample, respectively. By using

the values of  $E_t$ ,  $\nu_t$ , and  $\nu_s$  of 130 GPa, 0.18 [41], and 0.33 [43], respectively, the Young's moduli of the areas with the nanoparticle underneath and that of the surrounding area were calculated to be 6.6 GPa and 5.5 GPa, respectively. These calculations suggest that the subsurface Au nanoparticle buried 900 nm from the surface brought the Young's modulus on the area above the Au nanoparticle about 1.2 times higher than for the area without the nanoparticle underneath. It should be noted here that by using the second contact resonance mode or higher, more elaborated tip-sample model can be used to determine  $k^*$  and  $\gamma$  [16,42]. We performed AFAM imaging using the second resonance and confirmed that the buried Au nanoparticles can be visualized also by the second contact resonance (see Appendix C), but we found some spurious peaks in the frequency range around the second resonance which might be caused by the oscillation of the sample and/or cantilever holders. These spurious peaks hindered the resonance tracking by RT-AFAM and the fitting of the SHO model or the theoretical AFAM amplitude spectrum to the spectrum obtained by AFAM-CRS.

In this study, we have shown that the visualization is realized by the variation in the contact stiffness and damping of the polymer matrix, namely a higher contact stiffness and lower damping, due to the existence of the buried nanoparticles underneath. However, we do consider that the subsurface visualization mechanisms are not that simple. Actually we do not think that the features buried in such a deep subsurface can be visualized for every combination of the soft matrices and nanoparticles. For example, we attempted to visualize the similar samples prepared using the Au nanoparticles stabilized with surfactant molecules and dispersed in water. Despite the other conditions being the same as those described in this paper, we could not visualize the subsurface Au nanoparticles. We presume that the subsurface nanoparticle can be visualized only if the ultrasonic oscillation of the actuator was transmitted to the tip contact area without disturbance. Therefore, the subsurface feature visualization might be difficult for the nanoparticles with a surrounding layer of gases, liquids, or low-molecular materials that could disturb the transmission of the ultrasonic oscillation to the surface area under the tip.

#### 4. Conclusions

In this study, we visualized the subsurface Au nanoparticles of 40 nm diameter buried 900 nm in a polymer matrix from the surface using RT-AFAM and AFAM-CRS techniques, and discussed the subsurface feature visualization mechanisms. Both the RT-AFAM and AFAM-CRS results suggested that the subsurface features were visualized as the area with a higher contact resonance frequency and a higher  $Q$ -factor than those in the surrounding area, which means that the visualization is realized by the higher contact stiffness and lower damping of the polymer surface due to the existence of the buried nanoparticles underneath. The subsurface Au nanoparticle affects the contact stiffness and damping in the area whose diameter was smaller than that of the Au nanoparticle. We showed that RT-AFAM and AFAM-CRS techniques are powerful tools to investigate the effect of the subsurface features on the contact stiffness and damping. We plan to investigate the contact resonance on the samples with various combinations of the soft matrix and nanoparticle buried at various depths using these techniques for a full understanding of the subsurface imaging mechanisms by the AFM techniques utilizing the contact resonance in the near future.

#### Acknowledgment

This work was supported by Grant-in-Aids from the Japan Society for the Promotion of Science (JSPS).

## Appendix A.

### Relationship between the sweep time and the shape of the measured resonance spectrum

In general, the width of the resonance peak is often characterized by the full width of the frequencies at the half maximum power (FWHM), which is now defined as  $h$ . As the  $Q$ -factor of the contact resonance is defined as  $Q = f_c/h$ , we can rewrite  $h$  described as  $f_c/Q$ . If we sweep the excitation frequency with the sweep rate  $\nu_s$ , the sweep time ( $\Delta t$ ) for the frequency range of  $h$  is given by  $\Delta t = h/\nu_s = (f_c/Q)/\nu_s$ . As the amplitude and phase respond to the excitation signal with a delay on the order of the characteristic time constant ( $\tau_c$ ), which is given by  $\tau_c = 2Q/\omega_c = Q/\pi f_c$ , it is convenient to normalize the sweep time  $\Delta t$  by  $\tau_c$ . The normalized sweep time is therefore given by  $\pi(f_c/Q)^2/\nu_s$ .

Figure A1 shows the contact resonance amplitude spectra measured on the photopolymer sample when the tip was located in the area with the buried Au nanoparticle underneath (900 nm from the surface), taken at different sweep rates; i.e., 25 kHz/175 ms for (a), 25 kHz/116 ms for (b), and 25 kHz/35 ms for (c). The normalized sweep time were about 42, 29, and 10. While the amplitude spectrum in (a) was well fitted to the SHO model, as presented in figure 6(c), the spectra in (b) and (c) were distorted. Moreover, the resonance peak in figure A1(c) showed additional peaks on the right of the contact resonance peak due to transient responses.

## Appendix B.

### Histograms of $\Delta f$ , amplitude and $f_c$ images

Histograms of the  $\Delta f$  and amplitude images (shown in figures 3(b) and (c)) obtained by RT-AFAM, are shown in figure A2(a) and (b), respectively.  $\Delta f$  and amplitude values at the pixels “A”, “B”, and “C” indicated in figures 3(b) and (c) are located far out of the broad peaks representing the values at the other pixels, which represent that the contact stiffness and damping became much larger and smaller, respectively at these pixels.

Topography and  $f_c$  image of the area same as that in figure 4(a) are shown in figures A2(c) and (d), respectively.  $f_c$  image was obtained by fitting the contact resonance spectra by AFAM-CRS with the SHO model.  $f_c$  was largest at the pixel “1”, which is consistent with the frequency spectra shown in figure 4(b). Figure A2(d) shows a gradual increase of  $f_c$  during collection of the data from top to bottom of the image, which was caused by a gradual change in the loading force due to the thermal drift of the cantilever deflection because AFAM-CRS measurement took a long time as mentioned in Experimental section. The histogram of  $f_c$  in figure A2(d) is shown in figure A2(e). The largest  $f_c$  value (91.6 kHz), which is the value at pixel “1”, is apparently larger than its mean value of the histogram (90.1 kHz). These results indicate that subsurface Au particle brought large  $f_c$  at the pixel “1”.

## **Appendix C.**

### **AFAM imaging using the second contact resonance**

We prepare a sample with the same structure with a top-coat thickness of about 730 nm in the same way described in Section 2.1. A cantilever tip ( $k_z = 1.1$  N/m) was used for the AFAM imaging at the first and second resonance frequencies. Figure A3(a)-(c) are topography, AFAM amplitude and phase images obtained at 89.3 kHz which were set close to first contact resonance frequency. Figure A3(d)-(f) are those obtained at 224.5 kHz which were set close to second contact resonance frequency. In the phase images using the first and second resonances, we can find some bright features due to the buried Au nanoparticles, while the topographic images did not show any features at the corresponding areas. Note that the amplitude images also did not show any bright or dark features at the corresponding areas. This is because the excitation frequency was not correctly tuned despite that the contrast in AFAM amplitude image is very sensitive to the excitation frequency as presented in figure 5.

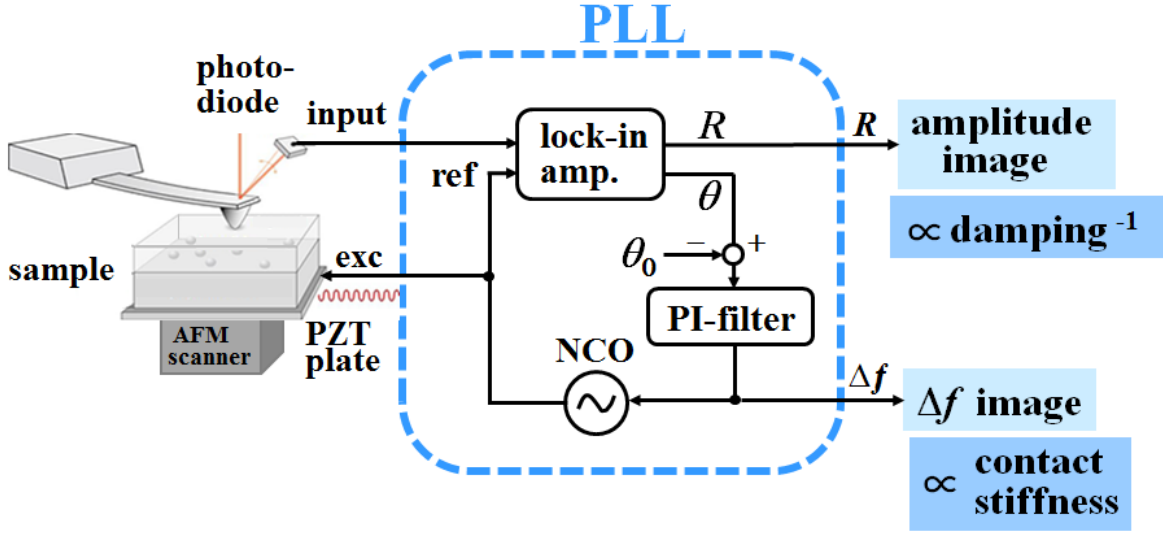
## References

- [1] Yamanaka K, Ogiso H, Kolosov O 1994 *Appl. Phys. Lett.* **64** 178-180.
- [2] Bodiguel H, Montes H, Fretigny C 2004 *Rev. Sci. Instrum.* **75** 2529-2535.
- [3] Shekhawat G S, Dravid V P 2005 *Science* **310** 89-92.
- [4] Tetard L, Passian A, Lynch R M, Voy B H, Shekhawat G, Dravid V and Thundat T 2008 *Appl. Phys. Lett.* **93** 133113.
- [5] Tetard L, Passian A, Venmar K T, Lynch R M, Voy B H, Shekhawat G, Dravid V P and Thundat T 2008 *Nature Nanotechnol.* **3** 501-505.
- [6] Yamanaka K, Kobari K and Tsuji T 2008 *Jpn. J. Appl. Phys.* **47** 6070-6076.
- [7] Shekhawat G, Srivastava A, Avasthy S, Dravid V 2009 *Appl. Phys. Lett.* **95** 263101.
- [8] Striegler A, Koehler B, Bendjus B, Roellig M, Kopycinska-Mueller M, Meyendorf N 2011 *Ultramicroscopy* **111** 1405-1416.
- [9] Hu S, Su C, Arnold W 2011 *J. Appl. Phys.* **109** 084324.
- [10] Killgore J P, Kelly J Y, Stafford C M, Fasolka M J, Hurley D C 2011 *Nanotechnol.* **22** 175706.
- [11] Spitzner E C, Riesch C, Magerle R 2011 *ACS Nano* **5** 315-320.
- [12] Ebeling D, Eslami B, Solares S D J 2013 *ACS Nano* **7** 10387-10396.
- [13] Verbiest G J, Zalm D J, Oosterkamp T H, Rost M J 2015 *Rev. Sci. Instr.* **86** 033704.
- [14] Kimura K, Kobayashi K, Matsushige K, Yamada H 2013 *Ultramicroscopy* **133** 41-49, in which AFAM was mistakenly referred to as UAFM.
- [15] Yamanaka K, Nakano S 1998 *Appl. Phys. A* **66** S313-S317.
- [16] Rabe U, Janser K, Arnold W 1996 *Rev. Sci. Instr.* **67** 3281-3293.
- [17] Rabe U, Kester E, Arnold W 1999 *Surf. Interface Anal.* **27** 386-391.
- [18] Cuberes M T, Assender H E, Briggs G A D, Kolosov O V 2000 *J. Phys. D: Appl. Phys.* **33** 2347-2355.
- [19] Kolosov O, Yamanaka K 1993 *Jpn. J. Appl. Phys.* **32** L1095-L1098.
- [20] Yamanaka K, Maruyama Y, Tsuji T, Nakamoto K 2001 *Appl. Phys. Lett.* **78** 1939-1941.

- [21] Kobayashi K, Yamada H, Matsushige K 2002 *Surf Interface Anal.* **33** 89-91.
- [22] Stan G, King S W, Cook R F 2012 *Nanotechnol.* **23** 215703.
- [23] Rodriguez B J, Callahan C, Kalinin S V, Proksch R 2007 *Nanotechnol.* **18** 475504.
- [24] Jesse S, Kalinin S V 2011 *J. Phys. D :Appl. Phys.* **44** 464006.
- [25] Gannepalli A, Yablon D G, Tsou A H, Proksch R 2011 *Nanotechnol.* **22** 355705.
- [26] Tsuji T, Kobari K, Ide S, Yamanaka K 2007 *Rev. Sci. Instrum.* **78** 103703.
- [27] Rabe U, Hirsekorn S, Reinstadtler M, Sulzbach T, Lehrer Ch, Arnold W 2007 *Nanotechnol.* **18** 044008.
- [28] Turner J A, Hirsekorn S, Rabe U, Arnold W 1997 *J. Appl. Phys.* **87** 966-979.
- [29] Rupp D, Rabe U, Hirsekorn S, Arnold W 2007 *J. Phys. D :Appl. Phys.* **40** 7136-7145.
- [30] Rabe U, Kopycinska M, Hirusekoln S, Saldana J M, Schneider G A, Arnold W 2002 *J. Phys. D: Appl. Phys.* **35** 2621-2635.
- [31] Hurley D C, Kopycinska-Muller M, Kos A B, Geiss R H 2005 *Meas. Sci. Technol.* **16** 2167-2172.
- [32] Passeri D, Bettucci A, Germano M, Rocci M, Arippi A, Sessa V, Fiori A, Tamburri E, Terranova M L 2006 *Appl. Phys. Lett.* **88** 121910.
- [33] Stan G, Price W 2006 *Rev. Sci. Instrum.* **77** 103707.
- [34] Kumar A, Rabe U, Hirsekorn S, Arnold W 2008 *Appl. Phys. Lett.* **92** 183106.
- [35] Wagner H, Bedolf D, Kuchemann S, Schwabe M, Zhang B, Arnold W, Samwer K 2011 *Nat. Mater.* **10** 439-442.
- [36] C I Enriquez-Flores, J J Gervacio-Arciniega, E Cruz-Valeriano, P de Urquijo-Ventura, B J Gutierrez-Salazar and F J Espinoza-Beltran 2012 *Nanotechnol.* **23** 495705.
- [37] Fukuma T, Kimura M, Kobayashi K, Matsushige K, Yamada H 2005 *Rev. Sci. Instrum.* **76** 053704.
- [38] Sader J E, Chon J W M, Mulvaney P 1999 *Rev. Sci. Instrum.* **70** 3967-3969.
- [39] Bozich D J 1966 *Shock and Vibration Bulletin* **35** 151-180.

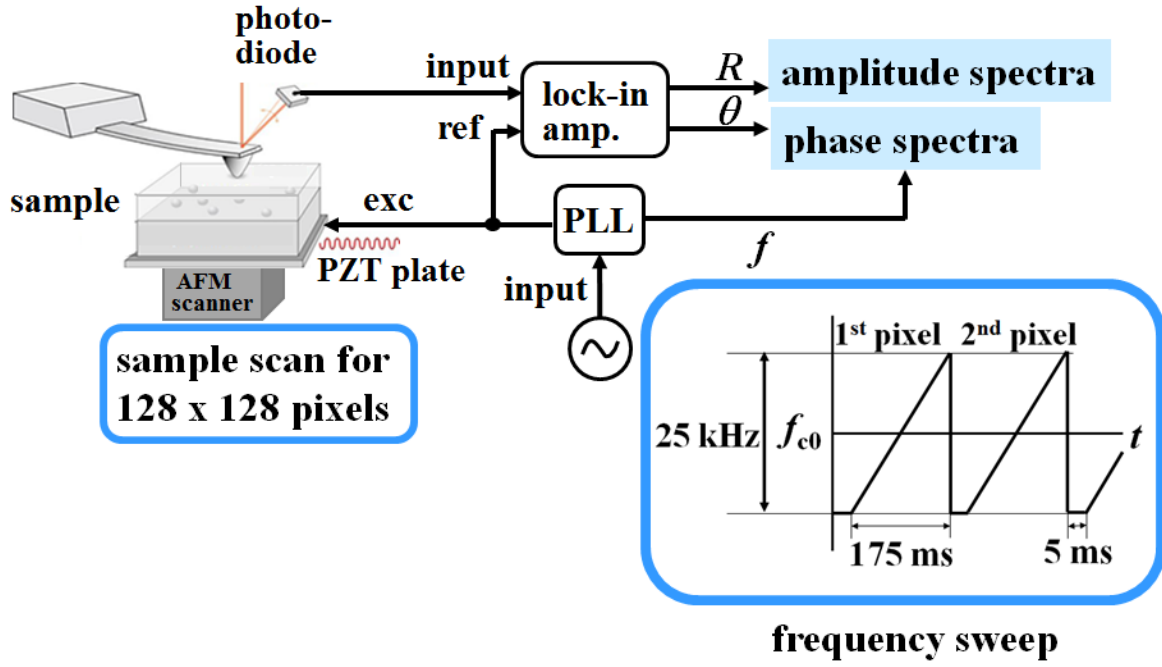


- [40] Gloth G and Sinapius M 2004 *Mech. Syst. Signal Proc.* **18** 1421-1441.
- [41] Rabe U, Amelio S, Kester E, Scherer V, Hirsekorn S, Arnold W 2000 *Ultrason.* **38** 430-437.
- [42] Yuya P A, Hurley D C, Turner J A 2008 *J. Appl. Phys.* **104** 074916.
- [43] Calabri L, Pugno N, Rota A, Marchetto D, Valeri S 2007 *J. Phys.: Condens. Matter* **19** 395002.



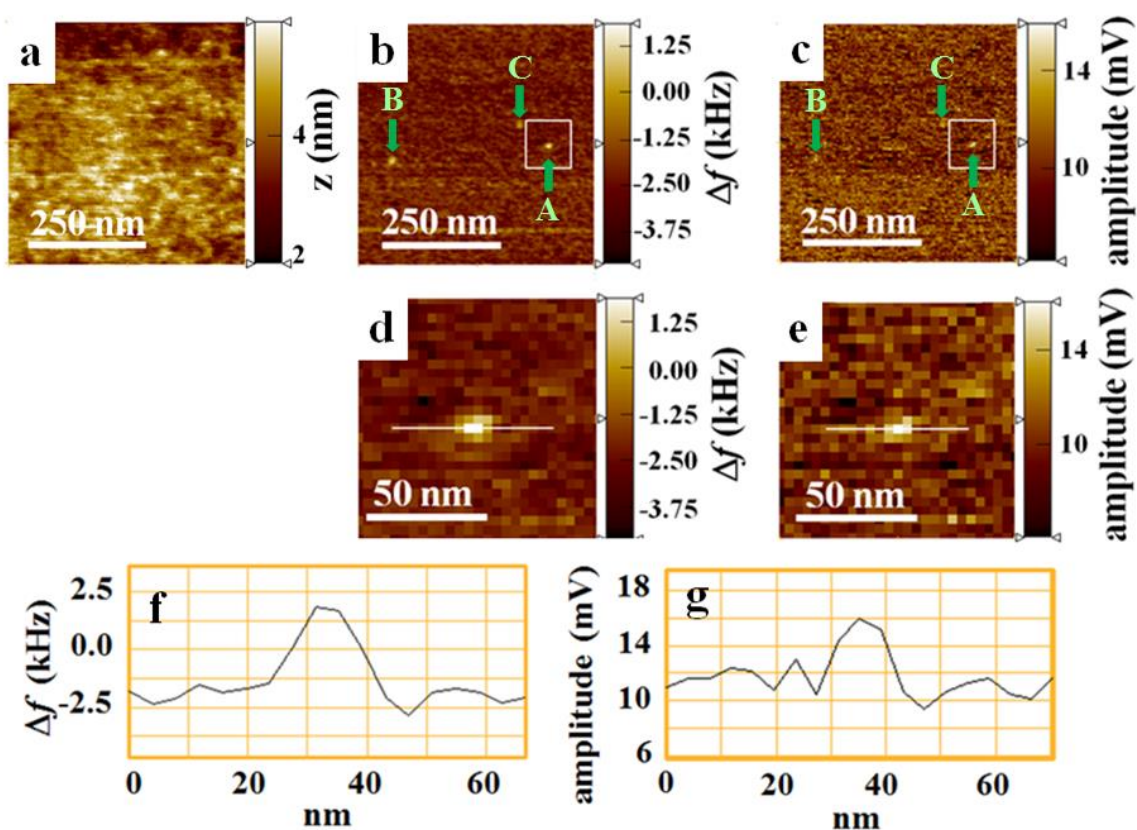
**Figure 1**

Figure 1: Experimental setup for RT-AFAM. PI-filter represents the proportional (P) and integral (I) filter. After contacting the tip to the sample surface, obtained the contact resonance frequency ( $f_{c0}$ ) at the initial contact point and phase difference ( $\theta_0$ ) between the signals of cantilever deflection and the excitation. While the tip was raster-scanned on the sample surface, the sample was oscillated with a constant amplitude using a piezoelectric actuator. The excitation frequency was controlled such that the phase difference ( $\theta$ ) was kept at the initial value  $\theta_0$ . The  $\Delta f$  signal ( $\Delta f = f - f_{c0}$ ) and amplitude signal ( $R$ ) at each pixel were recorded during a raster scan.



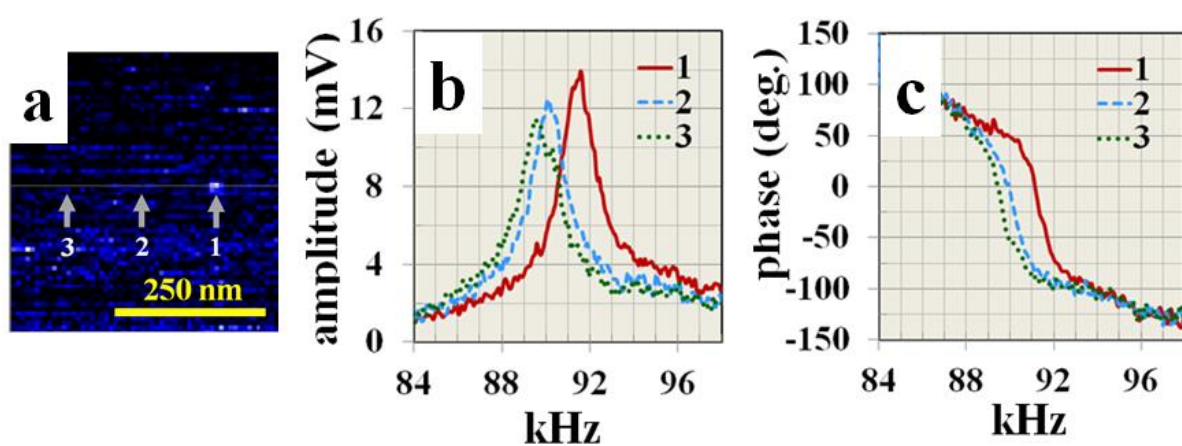
**Figure 2**

Figure 2: Experimental setup for AFAM-CRS. Amplitude and phase spectra were collected by applying a swept-sine signal to a piezoelectric actuator underneath the sample at every 128 x 128 pixels during a raster scan.



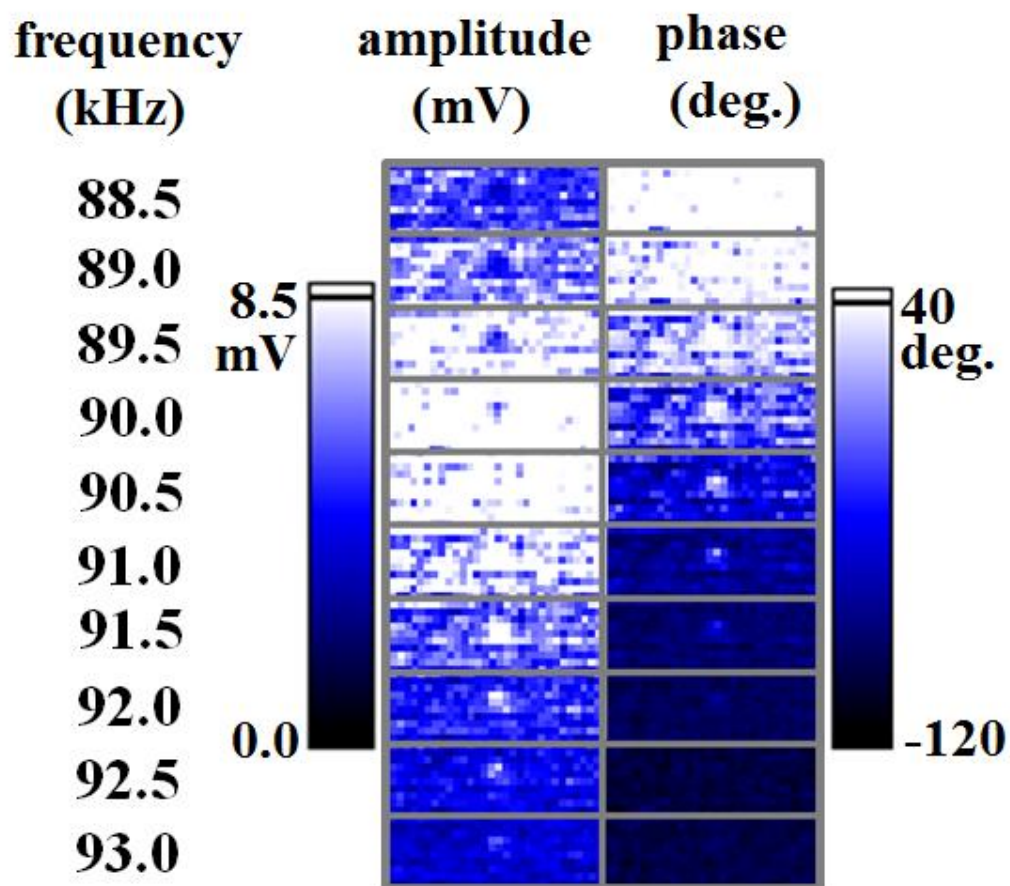
**Figure 3**

Figure 3: RT-AFAM images of a photopolymer sample in which Au nanoparticles of 40 nm in diameter were buried 900 nm from the surface; topographic image (a), frequency shift ( $\Delta f$ ) image (b), and amplitude ( $R$ ) image (c). (d) Magnified image of enclosed area shown in (b). (e) Magnified image of enclosed area shown in (c). (f) and (g) are cross-sectional profiles measured along the lines in (d) and (e), respectively.



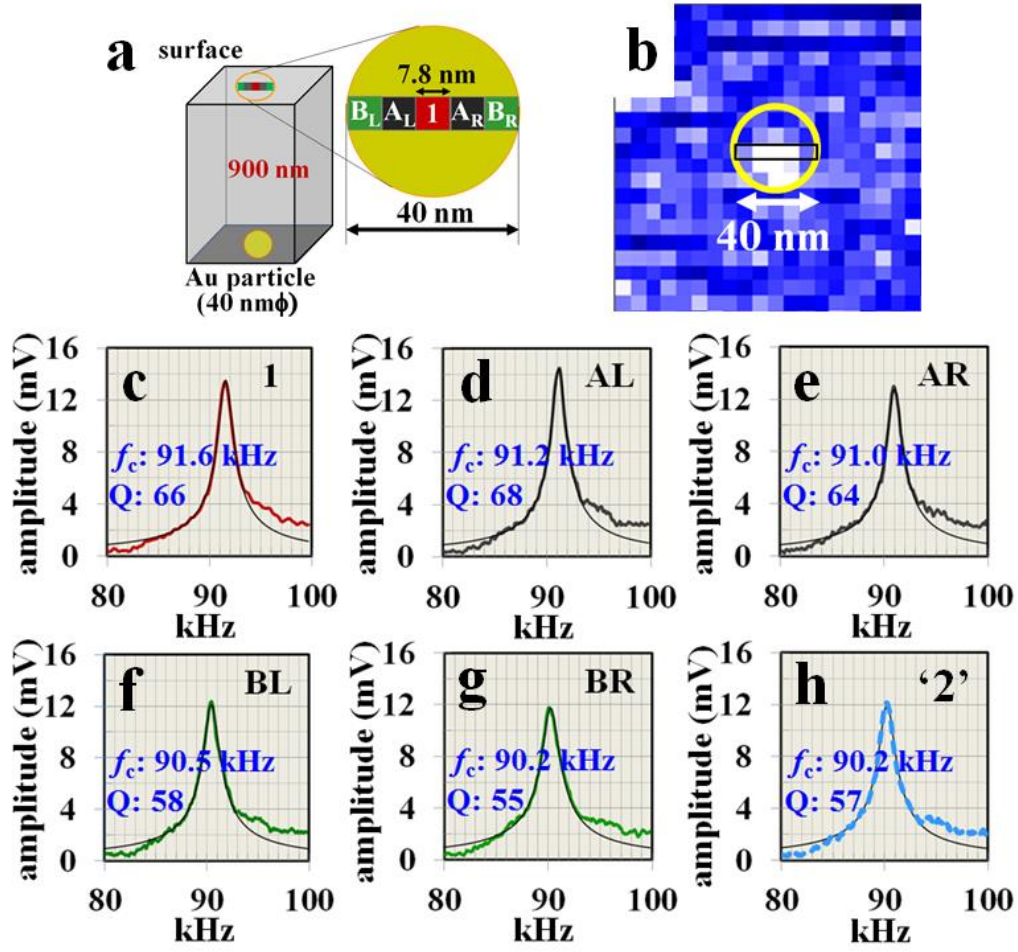
**Figure 4**

Figure 4: (a) AFAM amplitude image of a photopolymer sample with Au nanoparticles buried 900 nm from the surface, reconstructed from AFAM-CRS data at 91.7 kHz. The pixel numbered “1” corresponds to the brightest pixel. Pixels “2” and “3” are on the same scan line with pixel “1”. (b) and (c) show amplitude and phase spectra, respectively, obtained by AFAM-CRS on the pixels from “1” to “3” indicated in (a).



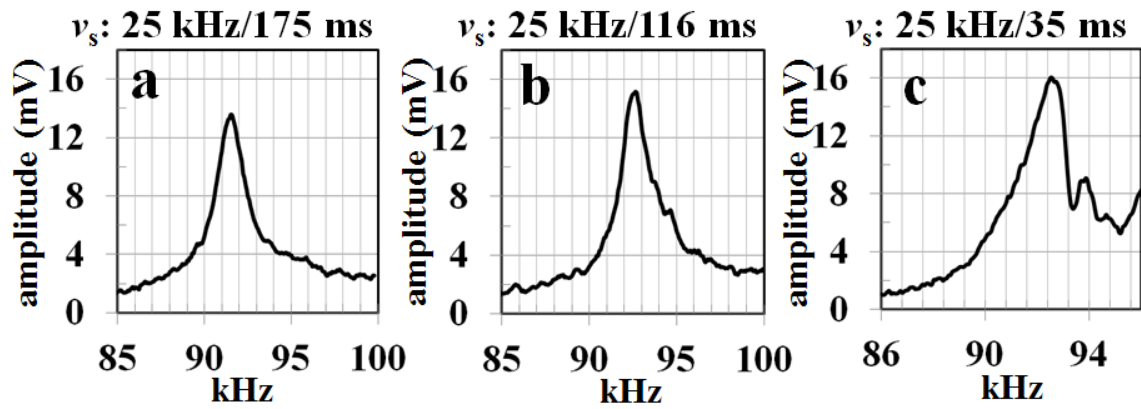
**Figure 5**

Figure 5: AFAM amplitude and phase images of a photopolymer sample with Au nanoparticles buried 900 nm from the surface reconstructed from AFAM-CRS data at frequencies ranging from 88.5 kHz to 93.0 kHz.



**Figure 6**

Figure 6: (a) Illustration of a polymer sample with a buried Au nanoparticle. The nanoparticle is supposed to exist just beneath the brightest pixel “1” in figure 4(a). (b) AFAM amplitude image reconstructed from AFAM-CRS data at 91.7 kHz (pixel size: 7.8 nm) (c)-(h) are amplitude spectra obtained by AFAM-CRS on pixels “1”, “A<sub>L</sub>”, “A<sub>R</sub>”, “B<sub>L</sub>”, “B<sub>R</sub>” in (a) and “2” in figure 4(a).



**Figure A1**

Figure A1: Contact resonance amplitude spectra taken at different sweep rates, which were measured on the photopolymer sample when the tip was located in the area with the buried Au nanoparticle underneath.



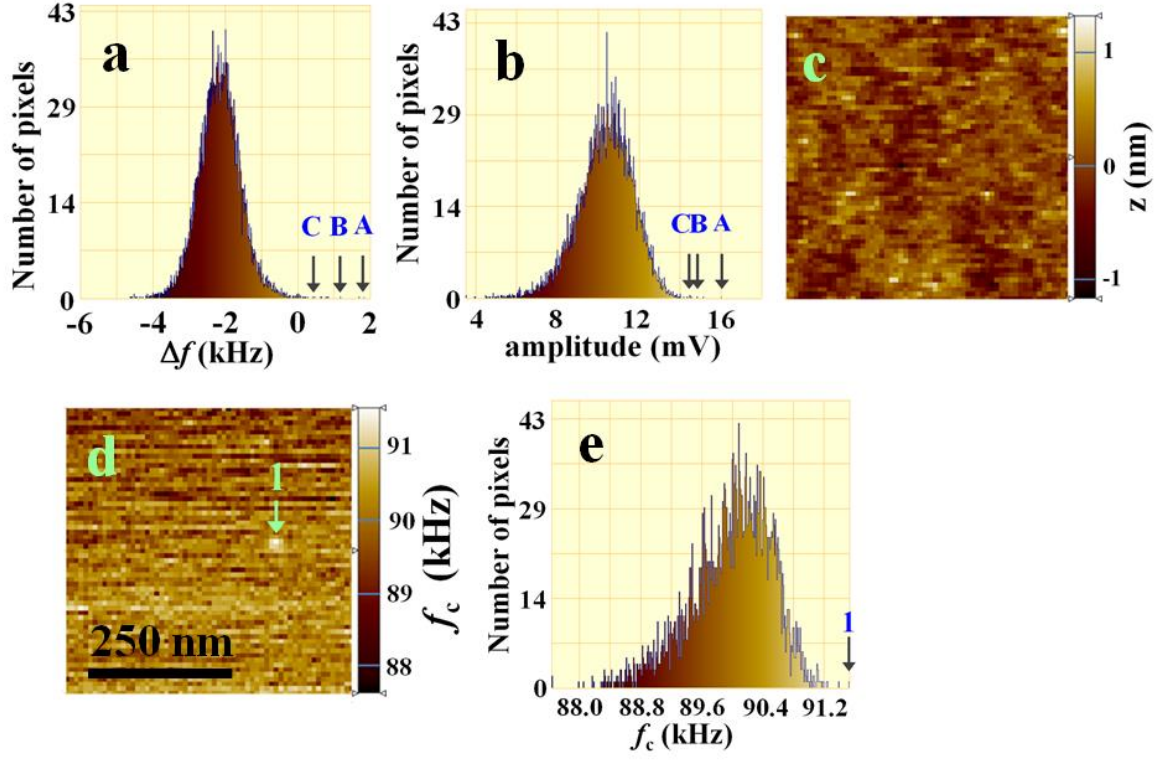


**Figure A2**

Figure A2: (a) Histogram of the  $\Delta f$  image (shown in figure 3(b)). (b) Histogram of the amplitude image (shown in figure 3(c)). (c) Topography for the area shown in figure 4(a). (d)  $f_c$  image for the area shown in figure 4(a). (e) Histogram of  $f_c$  image shown in (d).

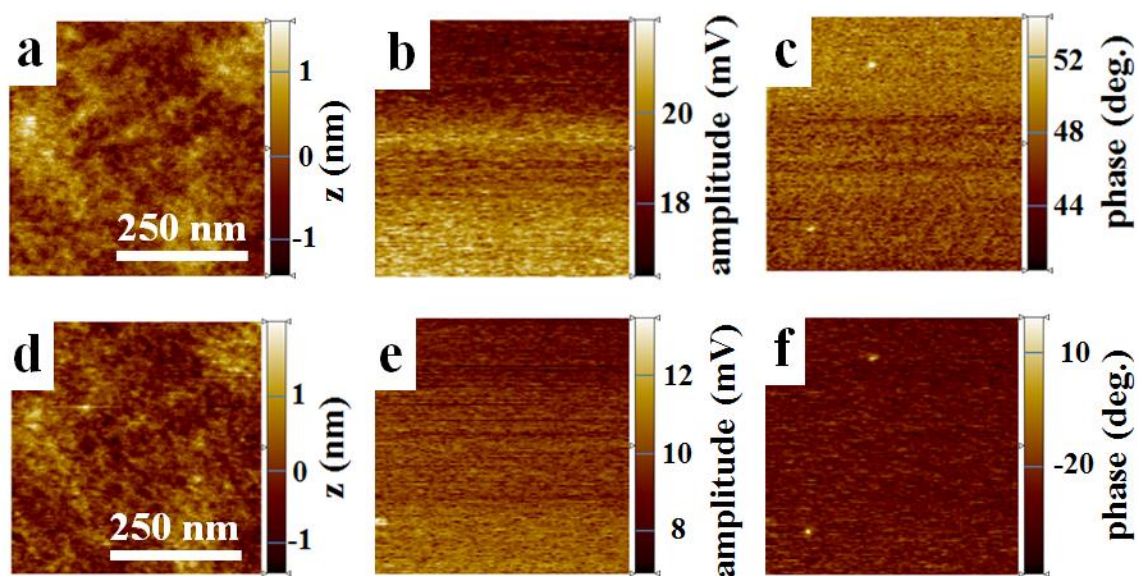


**Figure A3**

Figure A3: (a)-(c) are topography, AFAM amplitude and phase images obtained at 89.3 kHz which were set close to first contact resonance frequency. (d)-(f) are those obtained at 224.5 kHz which were set close to second contact resonance frequency.